

Diffusivity-Free Turbulence in Tabletop Rotating Rayleigh-Bénard Convection Experiments

Jewel A. Abbate (jewelabbate@ucla.edu)^a, Yufan Xu^{a,b}, Tobias Vogt^c, Susanne Horn^d, Keith Julien^e, Jonathan M. Aurnou^a

^aDepartment of Earth, Planetary, and Space Sciences, University of California, Los Angeles, CA, USA

^bPrinceton Plasma Physics Laboratory, Princeton University, Princeton, NJ, USA

^cInstitute of Fluid Dynamics, Helmholtz-Zentrum Dresden-Rossendorf, Dresden, Germany

^dCentre for Fluid and Complex Systems, Coventry University, Coventry, UK

^eDepartment of Applied Mathematics, University of Colorado, Boulder, CO, USA

arXiv:2411.11226v1 [physics.flu-dyn] 18 Nov 2024

Convection in planets and stars is predicted to occur in the “ultimate regime” of diffusivity-free, rapidly rotating turbulence, in which flows are characteristically unaffected by viscous and thermal diffusion. Boundary layer diffusion, however, has historically hindered experimental study of this regime. Here, we utilize the boundary-independent oscillatory thermal-inertial mode of rotating convection to realize the diffusivity-free scaling in liquid metal laboratory experiments. This oscillatory style of convection arises in rotating liquid metals (low Prandtl number fluids) and is driven by the temperature gradient in the fluid bulk, thus remaining independent of diffusive boundary dynamics. We triply verify the existence of the diffusivity-free regime via measurements of heat transfer efficiency Nu , dimensionless flow velocities Re , and internal temperature anomalies θ , all of which are in quantitative agreement with planar asymptotically-reduced models. Achieving the theoretical diffusivity-free scalings in desktop-sized laboratory experiments provides the validation necessary to extrapolate and predict the convective flows in remote geophysical and astrophysical systems.

Diffusivity-free (DF) turbulent convection is theorized to occur in the convection zones of stars and the fluid cores of planets, where it drives vortical flows, jets, and dynamo action that sustains global-scale magnetic fields (Moffatt and Dormy, 2019). The DF regime is characterized by strong turbulence dominated by fluid inertia, largely unaffected by the fluid’s micro-scale viscosity (ν) and thermal diffusivity (κ). For decades, researchers in the fluid physics and geophysics communities have sought to validate this theoretical regime through measurements of heat transfer efficiency in numerical simulations and laboratory experiments (e.g., Ahlers et al., 2009; Ecke and Shishkina, 2023). It remains an essential question whether the theoretical DF regime can be attained in a laboratory setting and be extrapolated to natural settings.

The canonical system for studying rotationally-constrained turbulent flows is the rotating Rayleigh-Bénard convection (RRBC) model (Ecke and Shishkina, 2023). In RRBC, a fluid layer confined between two parallel no-slip boundaries is heated from below and cooled from above while rotating

about its central vertical axis. Scaling laws that relate global heat transport (Nusselt number, Nu) and bulk flow velocity (Reynolds number, Re) to the buoyancy forcing (Rayleigh number, Ra), global rotation period (Ekman number, E), and material properties (Prandtl number, Pr) enable the extrapolation of laboratory-numerical findings to more extreme geophysical and astrophysical scales (Kraichnan, 1962; Spiegel, 1971; Stevenson, 1979; Christensen and Aubert, 2006; Plumley and Julien, 2019; Abbate and Aurnou, 2023). (See Table 1 for parameter definitions.)

The scaling predictions for the DF regime are derived by enforcing the constraint that thermal and viscous diffusion have no effect on the total heat transported through the system nor the internal flow velocities, and assuming that the system’s angular rotation rate goes to infinity ($\Omega \rightarrow \infty$) (Julien et al., 2012). The global heat transport prediction for rotating DF convection follows

$$Nu - 1 = C_J Ra^{3/2} E^2 Pr^{-1/2}, \quad (1)$$

where C_J is a constant prefactor. This value was determined by Julien et al. (2012) to be $C_J \approx 1/25$ in doubly-periodic planar models of the asymptotically reduced RRBC equations. Scaling predictions for the internal quantities are determined from

Table 1: Non-dimensional parameter definitions. Variables are ν (viscosity, m^2/s), κ (thermal diffusivity, m^2/s), α (thermal expansivity, $1/K$), g (gravitational acceleration, m/s^2), ΔT (vertical temperature drop, K), H (layer height, m), Ω (rotation rate, rad/s), q (total heat flux, W/m^2), k (thermal conductivity, $W/(mK)$), u (flow velocity, m/s).

Parameter	Definition	Meaning
Rayleigh	$Ra = \alpha g \Delta T H^3 / (\nu \kappa)$	thermal buoyancy diffusion
Ekman	$E = \nu / (2\Omega H^2)$	viscous diffusion
Prandtl	$Pr = \nu / \kappa$	Coriolis viscous diffusion
Nusselt	$Nu = qH / (k\Delta T)$	thermal diffusion total heat flux
Reynolds	$Re = uH / \nu$	conductive heat flux inertial advection
Rossby	$Ro = u / (2\Omega H) = ReE$	viscous diffusion inertial advection
Convective Rossby	$Ro_c = \sqrt{RaE^2 / Pr}$	Coriolis thermal buoyancy
Aspect ratio	$\Gamma = D/H$	Coriolis tank diameter tank height

a torque balance between the inertial and buoyancy terms of the vorticity equation describing rotating flows, neglecting viscous diffusion (e.g., Ingersoll and Pollard, 1982). Assuming any scaling coefficients other than C_J are order unity (see Methods), the prediction for the internal flow velocity is

$$Re = C_J^{2/5} Ro_c^2 E^{-1}, \quad (2)$$

and for the internal temperature fluctuation is

$$\theta/\Delta T = C_J^{3/5} Ro_c, \quad (3)$$

where θ is the root-mean-squared temperature perturbation, and $Ro_c = (RaE^2Pr^{-1})^{1/2}$ is the convective Rossby number (Abbate and Aurnou, 2023, and see Methods). These scalings have yet to be unambiguously found in any closed cell RRBC laboratory setup, thus raising the question of their applicability to any natural enclosed system (cf. Soderlund et al., 2014).

The fundamental barrier to achieving diffusion-free convection in RRBC lies in the physical boundaries through which heat is supplied and extracted. Boundary layers throttle energy transfer through the system. In most RRBC cases, the primary mode of convective instability is that of steady convection, which is thermally controlled by the conditions at the boundaries (King and Aurnou, 2012; Julien et al., 2016). The critical value of the Rayleigh number for which steady convective motions first develop (denoted as Ra_S , see Methods) is determined from a balance between friction and the Coriolis and

pressure gradient forces, such that the steady mode is considered a viscous convective instability (Zhang and Liao, 2017; Aurnou et al., 2018). Consequently, heat transfer in typical steady RRBC is dominated by boundary layer diffusion (e.g., Abbate and Aurnou, 2023; Oliver et al., 2023), which impedes the system from reaching the asymptotic DF scaling limit.

Lateral boundaries in RRBC give rise to additional sidewall-attached convective instabilities. These ‘‘wall modes’’ manifest as waves that travel azimuthally around the periphery of the tank, and are also a viscous instability (Ecke et al., 1992). Between contributions from steady and wall mode convection, RRBC heat transfer is often strongly influenced by diffusive effects.

In order to mitigate boundary contributions in convection studies, researchers have employed innovative techniques to bypass the boundaries altogether. Numerically, this has been achieved through the use of ghost layers or forced decoupling of boundary layers (Barker et al., 2014; Zou and Yang, 2021). Experimentally, radiative heat deposition directly into the fluid bulk (Lepot et al., 2018; Bouillaut et al., 2021) has recently found the asymptotic heat transfer scaling exponent, but a very different value of the prefactor than that of Julien et al. (2012) due to the differing means of thermal energy injection. Their results may apply to the rotating convective turbulence present in gas planets and stars; however, it is uncertain that they apply to terrestrial fluid environments where convection is still driven by fluxing heat through finite, solid boundaries. Thus, bounded

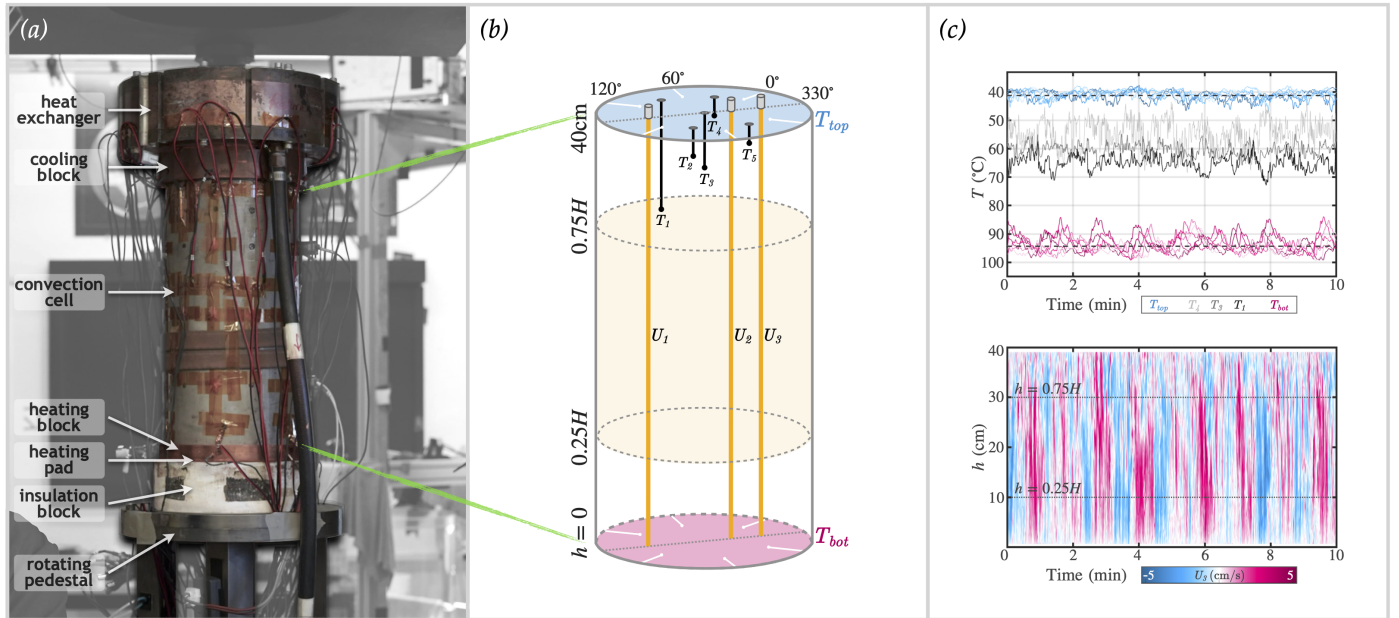


Figure 1: Rotating laboratory setup. (a) Image of the RoMAG device at UCLA with the $\Gamma \approx 1/2$ tank in place. Heat is supplied to the copper base (‘heating block’) by a heating pad and extracted from the copper lid (‘cooling block’) by a heat exchanger routed to a recirculating chiller. The cell is filled with liquid gallium and wrapped in layers of insulation (not pictured). Red and black visible wires are connected to thermistors and Doppler transducer probes. (b) Schematic of measurement locations. White lines at the cell boundaries represent thermistors embedded within the heating and cooling blocks used to measure ΔT . Black dots indicate the location of five internal thermistors used to measure temperature fluctuations, θ . Orange lines indicate the 1D path sensed by Doppler transducers used to measure vertical flow velocity, u_z . (c) Example time series data for a turbulent case in the oscillatory regime. The top panel shows thermistor data, where shades of pink (blue) indicate bottom (top) boundary temperatures and shades of gray indicate internal temperatures. The bottom panel shows velocimetry data, where pink (blue) regions indicate upward (downward) flow. The middle 50% of the chord is used to calculate the rms-velocity, which is demarcated with dotted lines here and in panel (b). The case shown corresponds to parameters: $Ra \approx 10^9$, $E \approx 8 \times 10^{-7}$, $Ro_c \approx 0.16$, $Ro_z \approx 0.01$, and $Re_z \approx 2 \times 10^4$.

RRBC systems have yet to yield unambiguous asymptotic scalings, raising the dual concerns *i*) that standard laboratory-scale devices may be unable to realistically simulate geophysical turbulence or *ii*) that DF scalings do not exist in natural convection enclosed by solid boundaries (Favier and Knobloch, 2020; de Wit et al., 2020; Zhang et al., 2021; Lu et al., 2021; Madonia et al., 2023).

To address these questions, we utilize the thermal-inertial oscillatory mode of convection that exists in low Pr liquid metal RRBC (Chandrasekhar, 1961; Zhang and Roberts, 1997; Zhang and Liao, 2009; Horn and Schmid, 2017; Aurnou et al., 2018). Contrary to steady convection, which is subject to thermal boundary conditions, oscillatory convection is driven entirely by the internal temperature field. Zhang and Roberts (1997) showed that oscillatory convection is described by a thermal-inertial wave, arising from a balance between inertia and Coriolis acceleration, with no dependence on the nature of the boundaries or diffusive effects at dominant order. This thermally-driven inertial instability arises exclusively in rotating low $Pr < 0.68$ fluids, like liquid metals and plasmas. The critical Ra for which oscillatory modes onset (denoted as Ra_O , see Methods) occurs at lower Ra than that for steady convection (Ra_S), such that thermal-inertial oscillations are considered the preferred mode of convection when the Prandtl number is sufficiently small (Zhang and Liao, 2017). Here, by isolating the oscillatory mode in rotating liquid gallium ($Pr \approx 0.027$) convection experiments, we show that the inertial asymptotic DF scalings (1) - (3) can be realized in a desktop-sized RRBC cell, and are in good quantitative agreement with Julien et al. (2012)'s asymptotically-reduced RRBC models, further validating both laboratory and multi-scale asymptotic methods.

UCLA's RoMAG device is used to conduct our experiments. The setup (Fig. 1a and Supplementary Fig. 4a) features a right cylindrical convection cell with a height of $H = 40.0$ cm and a diameter of $D = 19.9$ cm, yielding an aspect ratio of $\Gamma = D/H \approx 1/2$. The cell is constructed with a stainless steel sidewall positioned between two copper end blocks. Heat is supplied through a basal heating pad, while a heat exchanger plate, connected to a re-circulating chiller, removes heat at the top. After equilibration, both the top and bottom copper end blocks are maintained at fixed temperatures for the duration of the experiment. The convection cell is affixed to a rotating platform that spins the cell about its vertical axis. We carry out a systematic survey, varying the Rayleigh and Ekman numbers by approximately two orders of magnitude each ($8 \times 10^6 < Ra < 1 \times 10^9$ and $3 \times 10^{-7} < E < 1 \times 10^{-5}$).

For each experiment, we acquire measurements of temperature, heat flux, and velocity. Thermistors embedded within the top and bottom thermal blocks measure the vertical temperature gradient, ΔT (see white lines in Fig. 1b and pink/blue time series lines in Fig. 1c). Five internal thermistors are positioned within the bulk fluid to measure the internal temperature fluctuations (see black lines in Fig. 1b and black/gray time series lines in Fig. 1c). The standard deviation of each internal thermistor time series is calculated to determine the local perturbation at each location, which are then RMS-averaged to yield θ . Vertical flow velocity, u_z , is measured using an ultra-

sonic Doppler velocimeter (UDV). A Doppler transducer probe is positioned in contact with the interior fluid, oriented along the vertical axis of the cylinder. Natural impurities in the gallium act as particles that the UDV can acoustically sense (Wang and Kelley, 2021). Velocities are recorded at approximately 2 mm increments across the entire vertical length of the cell at a sampling rate of approximately 10 Hz. The characteristic u_z velocity is then calculated as a time- and space-RMS, using the

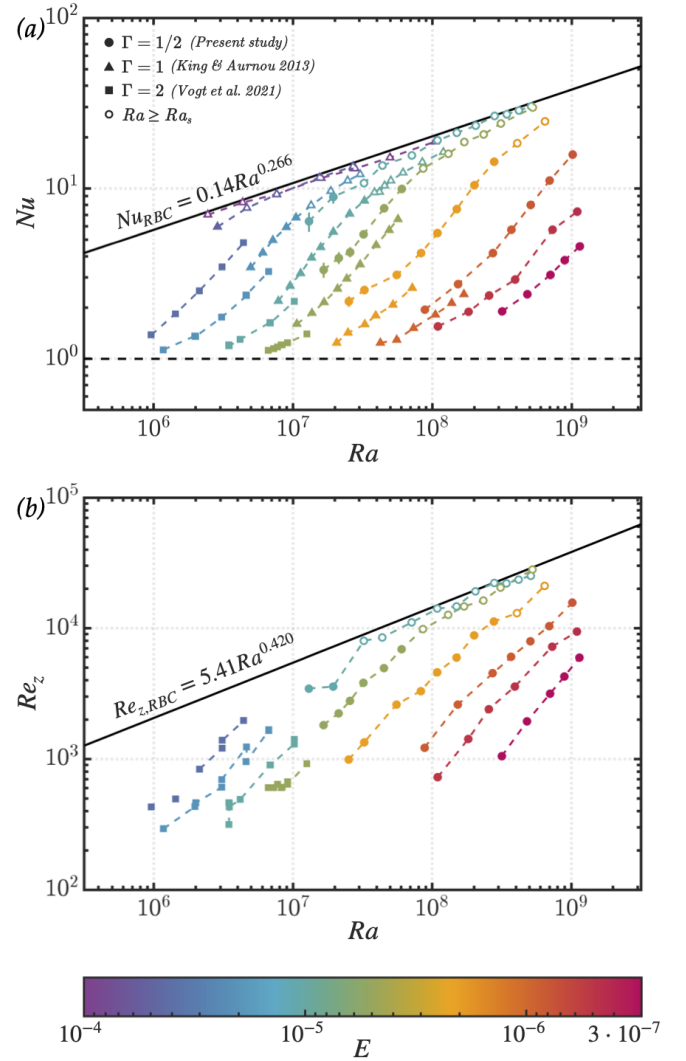


Figure 2: Rotating convection survey measurements. (a) Global heat transport efficiency, Nu , and (b) vertical non-dimensional bulk velocity, Re_z , as a function of thermal buoyancy forcing, Ra . Symbol color denotes the Ekman number, E , where red (lowest E) indicates the strongest Coriolis forcing and purple (highest E) indicates weaker Coriolis forcing. Symbol shape denotes the cell aspect ratio, $\Gamma = D/H$. Laboratory results from this study ($\Gamma \approx 1/2$) are marked as circles, those from King and Aurnou (2013) ($\Gamma \approx 1$) are marked as triangles, and those from Vogt et al. (2021) ($\Gamma \approx 2$) are marked as squares. Hollow points indicate cases in which the steady mode of convection has onset ($Ra \geq Ra_S$), which is used here as a transition point between inertial and steady convection regimes. The solid black line in each panel shows the non-rotating empirically-determined scaling for the $\Gamma \approx 1/2$ cell from this study for reference. A plot of the non-rotating RBC data used to generate these fits is shown in Supplementary Fig. 5. The full data set can be found in Supplementary Table 3.

middle 50% of the cell height (see orange lines and light orange area shaded in Fig. 1b and the Hovmöller diagram in 1c). The equations used for averaging are included in Methods.

We compare our $\Gamma \simeq 1/2$ convection cell results to those of two other aspect ratios from prior studies performed using the same experimental device. King and Aurnou (2013) conducted rotating convection experiments in liquid metal using a $\Gamma \simeq 1$ cell, measuring global heat transport efficiency, Nu , with their data reported in King and Aurnou (2015). Vogt et al. (2021) conducted experiments using a $\Gamma \simeq 2$ cell, measuring the Nusselt number, Nu , vertical Reynolds number, Re_z , and internal temperature fluctuations, θ . We additionally compare our findings to the asymptotically-reduced planar models of Julien et al. (2012) by incorporating their best-fit prefactor $C_J = 1/25$ in the heat transfer prediction (1). We elect to carry this prefactor through the asymptotic predictions for the Reynolds number (2) and thermal anomalies (3), as shown in Methods.

Fig. 2 presents the measured heat transfer (Nu) and vertical velocities (Re_z) across all three aspect ratios considered, plotted as a function of the buoyancy forcing (Ra). Rotating data are indicated by colored markers, while a solid black line represents the empirically determined non-rotating scaling relation (data shown in Supplementary Fig. 5). Solid colored points indicate data within the oscillatory convection regime. Hollow points represent experiments where steady convection has additionally onset, following $Ra \geq Ra_S = (8.70 - 9.63E^{1/6})E^{-4/3}$ (Niiler and Bisshopp, 1965; Kunnen, 2021). These cases are not expected to follow the inertial DF scaling predicted for the oscillatory mode (see Supplementary Fig. 6) and are therefore not included in the scaling analysis. Additionally, in low Prandtl number fluids, a weakly nonlinear regime is present near onset ($1 \leq Ra/Ra_0 \lesssim 1.5$) (Jones et al., 1976; Chiffaudel et al., 1987). Thus, only measurements where $Ra/Ra_0 > 1.5$ are considered here. Notably, all cases exhibit high Reynolds numbers with $300 \lesssim Re \lesssim 3000$. Even near convective onset ($Nu \leq 2$), the Reynolds numbers reach as high as $Re \approx 10^3$.

Fig. 3 compares our measurements with the theoretical DF predictions formulated with Julien et al. (2012)'s $C_J = 1/25$ prefactor. The data is presented as colored markers, with a solid black line indicating the asymptotically reduced predictions. Power law fits to the oscillatory data (solid points) are shown as dotted lines of the same color. Inset plots display the best-fit values, and Table 2 lists the specific best-fit power law relations for each dataset. Pre-factors and exponents of unity, which are marked by a solid black horizontal line in the inset plots, correspond to the asymptotically reduced result. The oscillatory data is in good quantitative agreement with this prediction. Hollow points (indicating $Ra > Ra_S$) clearly deviate from the diffusion-free scaling. Thus, the thermal-inertial modes follow the non-diffusive scalings, whilst the inclusion of bulk stationary modes truncates this behavior.

The heat transfer efficiency (Nu) results in Fig. 3a show a close fit between the asymptotically reduced and $\Gamma \simeq 2$ cell data. Decreasing the aspect ratio likely introduces strong wall mode effects that enhance global heat transfer efficiency (Favier and Knobloch, 2020; de Wit et al., 2020; Zhang et al., 2021; Lu et al., 2021), causing the slope to deviate from the asymptotic

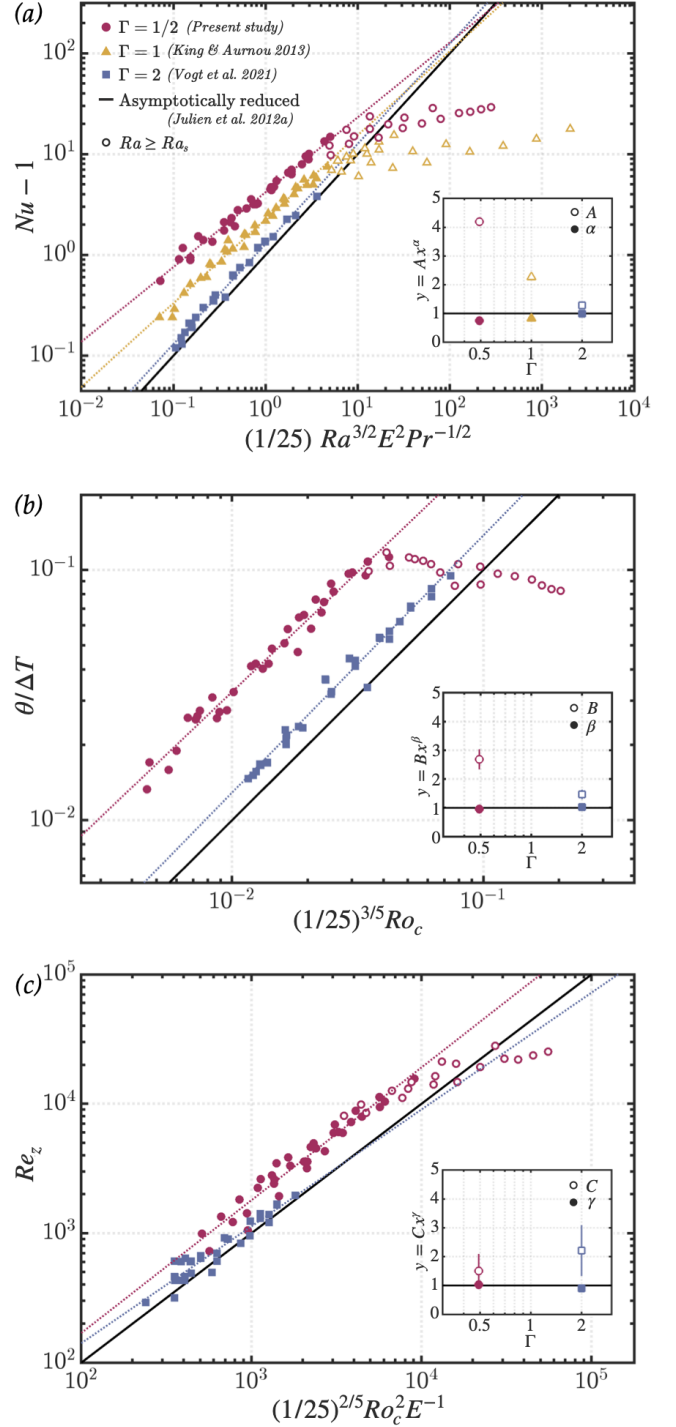


Figure 3: Laboratory scaling results. (a) The convective heat flux relative to conductive heat flux, $Nu - 1$, (b) the normalized internal temperature perturbation, $\theta/\Delta T$, and (c) the measured vertical Reynolds number, Re_z , each shown as a function of the asymptotically reduced scaling result from Julien et al. (2012) (see Methods for details). Solid black lines indicate the asymptotically reduced predictions. Dotted lines show the best-fit power law results to each Γ data set, where the hollow points (indicating $Ra/Ra_S \geq 1$) are excluded from the fit. The inset plots display the best-fit prefactors as hollow symbols and the best fit scaling exponents as solid symbols, with solid horizontal lines marking the asymptotic predictions. The best-fit scaling relations are each listed in Table 2. Across all three measured quantities, the scaling approaches the asymptotic result as the aspect ratio, Γ , increases. Other markers are the same as those in Fig. 2.

scaling. The inset plot, which shows the best-fit values, reveals a clear trend toward the asymptotic limit as the aspect ratio increases for both the scaling exponent and the prefactor. Thus, the wider aspect ratio cell more closely replicates infinite plane layer behavior than the narrower aspect ratio cells, making it a better fit to the asymptotically reduced model result.

The thermal anomaly (θ) results shown in Fig. 3b exhibit excellent agreement with theory across both aspect ratios ($\Gamma \approx 1/2$, $\Gamma \approx 2$). The inset plots show scaling exponents near unity for both datasets. Unlike global heat transfer, internal fluctuations appear to be insensitive to wall flow behaviors such that they exclusively follow the thermal-inertial bulk scaling trends regardless of aspect ratio.

The vertical velocity Re_z results shown in Fig. 3c also strongly align with diffusion-free theory, as they are similarly unaffected by wall modes. Overall, we find simultaneous agreement with diffusion-free predictions across all three independently measured quantities in this study: thermal anomalies in the bulk, velocities in the bulk, and global heat transfer. Further, we find increasing fidelity of this agreement in higher aspect ratio containers.

These experiments show that diffusion-free physics can exist even in relatively small, closed containers of rotating fluid. Of specific note, we find that rotating low Pr liquid metal convection in a short, wide aspect ratio tank ($\Gamma \approx 2$) robustly agrees with the varied Pr results of the asymptotically-reduced planar modeling study of Julien et al. (2012). This work thus verifies the C_J constant found by Julien et al. (2012) to hold for DF planar systems with no-slip top and bottom boundaries. In our laboratory setup, we utilize the oscillatory regime of low Pr rotating convection to achieve this goal. However, Julien et al. (2012) find that the scaling can hold for a range of Pr assuming the criteria of rotationally-constrained turbulence are met ($Ro \ll 1 \ll Re$), as expected in planetary interior flows (Holme et al., 2015; Soderlund et al., 2024) and in many stellar settings as well (Vasil et al., 2021).

The laboratory-theoretical agreement crucially validates application of DF theory to natural settings. Here we consider Earth's outer core as an example. Scalings (1) - (3) are cast in terms of the superadiabatic temperature difference, ΔT , where a known Rayleigh number or convective Rossby number is used to predict an unknown heat transfer, velocity, and thermal anomaly. However, the Rayleigh number is rarely known in geophysical or astrophysical applications; instead, a heat flux or flow velocity is typically estimated from observational data. Specifically for Earth's outer core, flow velocities are estimated from geomagnetic secular variation to be $u \approx 5 \times 10^{-4}$ m/s (Holme et al., 2015), which gives a Reynolds number of $Re \approx 10^9$. The diffusion-free Reynolds number equation (1) can then be converted to a flux-based format and rearranged to solve for the Rayleigh number as an unknown quantity:

$$Ra = C_J^{-2/5} Re E^{-1} Pr. \quad (4)$$

Using (4) with $C_J = 1/25$, $Re \approx 10^9$, $E \approx 10^{-15}$, and $Pr \approx 0.1$ for Earth's outer core, the Rayleigh number is calculated to be $Ra \approx 4 \times 10^{23}$. The Rayleigh number estimate can then be used

Table 2: Power law fits corresponding to the data shown in Fig. 3. Prefactors (A , B , C) and exponents (α , β , γ) of unity correspond to the result of the plane layer asymptotically reduced models of (Julien et al., 2012).

$Nu - 1 = A \left[(1/25) Ra^{3/2} E^2 Pr^{-1/2} \right]^\alpha$		
Γ	A	α
1/2	4.20 ± 0.08	0.74 ± 0.02
1	2.26 ± 0.05	0.83 ± 0.02
2	1.29 ± 0.03	0.99 ± 0.02
$\theta/\Delta T = B \left[(1/25)^{3/5} Ro_C \right]^\beta$		
Γ	B	β
1/2	2.69 ± 0.35	0.96 ± 0.03
2	1.46 ± 0.16	1.03 ± 0.03
$Re_z = C \left[(1/25)^{2/5} Ro_C^2 E^{-1} \right]^\gamma$		
Γ	C	γ
1/2	1.50 ± 0.58	1.03 ± 0.04
2	2.21 ± 0.88	0.90 ± 0.05

to determine the superadiabatic temperature differential ΔT in the core following $\Delta T = Ra \cdot \nu \kappa / (\alpha g_{cmb} H^3) \approx 3$ mK, where $\nu \approx 10^{-6}$ m²/s, $\kappa \approx 10^{-5}$ m²/s, $\alpha \approx 1.2 \times 10^{-5}$ 1/K, $g_{cmb} \approx 10.68$ m/s, and $H \approx 2255$ km (Olson, 2015). Using (3), the temperature anomaly is calculated as $\theta = (1/25)^{3/5} (Ra E^2 Pr^{-1})^{1/2} \Delta T \approx 10^{-6}$ K.

Equation (4) can additionally be coupled with the heat transfer prediction (1) to estimate the power driving thermal convection in the core (neglecting compositional effects). We multiply both sides of (1) by the Rayleigh number to solve for the flux Rayleigh number, $Ra_F = Ra(Nu - 1) = \alpha g q_{conv} H^4 / (\nu \kappa k)$, where q_{conv} is the convective heat flux, leading to the expression:

$$Ra_F = C_J Ra^{5/2} E^2 Pr^{-1/2}. \quad (5)$$

By substituting the Rayleigh number prediction into (5), we calculate a flux Rayleigh number of $Ra_F \approx 10^{28}$ in Earth's core. Further substituting $k \approx 100$ W/(mK) (Olson, 2015) and solving for q_{conv} yields a prediction of $q_{conv} \approx 3$ mW/m² for the core. The superadiabatic heat flow is then calculated as $Q_{conv} = q_{conv} \cdot 4\pi r_{cmb}^2 \approx 0.5$ TW driving thermal convection in the core, where $r_{cmb} \approx 3480$ km is the radius of the core mantle boundary. These predictive equations can be applied in other geophysical settings as well, such as subsurface oceans (e.g., Soderlund et al., 2024).

Measurements of the inertial oscillation-dominated range of liquid metal RRBC in closed cylindrical laboratory containers reveal that asymptotic DF heat and momentum transfer can be realized on the laboratory scale. We observe these trends in measurements of internal flow velocities and thermal fluctuations regardless of tank geometry. In contrast, global heat transfer is significantly influenced by wall modes in narrow, low aspect ratio cells, with asymptotic trends predominantly found in wide, high aspect ratio cells that better resemble plane layer geometry. If wall modes can be suppressed (cf. Terrien

et al., 2023), it may be possible to achieve asymptotic heat transfer scalings in taller, more slender $\Gamma \lesssim 1$ tanks. It may be possible to further investigate DF scaling behaviors using lower Pr fluids, such as liquid sodium, in which Ra_S/Ra_O attain larger values. By verifying here that diffusivity-free convection exists in a standard desktop-scale RRBC experimental cell, it is now possible to accurately and confidently model the convective turbulence that exists in rapidly rotating planetary and stellar interiors.

Data and Code Availability

All data generated or analyzed during this study are included in this article (and its supplementary information). Custom code is not used in the analysis of the data.

Author Contributions

J.A.A. and J.M.A. conceived the idea for the study; Y.X. constructed this iteration of the experimental device; J.A.A. and Y.X. conducted all laboratory experiments; T.V. contributed to Doppler data collection; J.A.A. conducted the data analysis; J.A.A., S.H., K.J., and J.M.A. conducted the theoretical analysis; J.A.A. and J.M.A. wrote the original manuscript with revisions contributed by Y.X., T.V., and S.H.

Methods

Experimental device. The laboratory device used here, RoMAG, has been used in a number of previous liquid metal convection studies (King and Aurnou, 2013, 2015; Aurnou et al., 2018; Vogt et al., 2018, 2021; Grannan et al., 2022; Xu et al., 2022, 2023), two of which produced results included in Fig. 2 and Fig. 3 for analysis (King and Aurnou, 2015; Vogt et al., 2021). For the new data acquired in this study, the setup consists of a right cylindrical cell of inner diameter $D = 2R = 19.68$ cm and height $H = 40$ cm to yield an aspect ratio of $\Gamma = D/H = 0.49$. The cell sidewall is made of stainless steel, the top and bottom plate boundaries are made of copper, and the working fluid is liquid gallium ($Pr \approx 0.027$). Layers of aerogel insulation (approximately 3 cm thick total) surround the cell sidewall, while a 7.62 cm thick calcium silicate insulation block sits below the lower plate boundary to mitigate heat losses. A non-inductively wound electrical heating pad at the bottom of the cell supplies a fixed flux of heating power ranging from $P = 10$ to 2000 W, while the top of the cell is maintained at a fixed temperature using a recirculating chiller. The generated temperature gradients range from approximately $\Delta T = 1$ to 60 K. The cell is mounted on a platform that rotates at rates ranging from $\Omega = 0.105$ to $\Omega = 3.67$ rad/s (1 to 35 revolutions per minute). A systematic survey was performed such that the Rayleigh and Ekman numbers each vary by approximately two orders of magnitude ($8 \times 10^6 < Ra < 1 \times 10^9$ and $3 \times 10^{-7} < E < 1 \times 10^{-5}$).

Data acquisition. Twelve thermistors are located within the top and bottom plate boundaries to measure the global temperature gradient,

$$\Delta T = \bar{T}_{bot} - \bar{T}_{top}, \quad (6)$$

which is used in the calculation of the Rayleigh and Nusselt numbers (e.g., King et al., 2012; Xu et al., 2022; Abbate and Aurnou, 2023). Six thermistors contribute to each the top and bottom boundary temperature calculation following

$$\bar{T}_{top, bot} = \frac{1}{6N_t} \sum_{i=1}^6 \sum_{j=1}^{N_t} T_{ij} \pm \frac{\bar{q}d}{k_{Cu}}, \quad (7)$$

where \bar{T}_{top} is determined using only sensors in the top plate, \bar{T}_{bot} is determined from those in the bottom, and N_t is the length of the time series. The thermistors are embedded within the copper plates at a location $d = 2$ mm away from the fluid-plate interface, so the measured temperature is adjusted to correct for conduction over length d via the second term in (7), where \bar{q} is the time-averaged heat flux given by (11) and k_{Cu} is the thermal conductivity of the copper plate. The temperature-dependent fluid material properties are calculated using the mean temperature,

$$\bar{T} = (\bar{T}_{bot} + \bar{T}_{top})/2. \quad (8)$$

The input heat flux, $q_{in} = P_{in}/A$, is set by the power supply where P_{in} is the wattage of the input heating power and A is the active surface area of the fluid-plate interface. This value

is confirmed with measurements of current, I , and voltage, V , at the location of the heating pad to calculate $P_{in} = IV$. Thermistors located within the layers of aerogel insulation are used to measure the heat lost through the cell sidewall. This loss is calculated as

$$P_{sw,loss} = \frac{2\pi k_{ins} H (T_{sw} - T_{ins})}{\log(R_{ins}/R_{sw})}, \quad (9)$$

where k_{ins} is the thermal conductivity of aerogel, T_{sw} is the temperature measured at cell sidewall, T_{ins} is the temperature measured after one layer of insulation, R_{sw} is the radial position of the sidewall thermistor, and R_{ins} is the radial position of the insulation thermistor. This loss is subtracted from the power measured at the location of the heating pad. Some power is additionally lost to vertical conduction through the stainless steel sidewall. This is estimated via

$$P_{sw,cond} = \frac{\pi(R_{sw}^2 - R^2)k_{sw}\Delta T}{H}, \quad (10)$$

where R is the inner radius of the cylinder and k_{sw} is the thermal conductivity of the stainless steel sidewall. The total heat flux through the fluid is thus

$$\bar{q} = \frac{\bar{P}_{in} - \bar{P}_{sw,loss} - \bar{P}_{sw,cond}}{\pi R^2}, \quad (11)$$

where each overlined quantity is time-averaged. This \bar{q} is then used in the calculation of the Nusselt number.

Five internal thermistors are located within the fluid interior of the cell to measure bulk temperature fluctuations, θ . Internal thermistor locations are shown in Fig. 1b and Supplementary Fig. 4b. Each internal thermistor measures the local temperature at its respective location over the course of the experiment. The standard deviation of the temperature time series provides the thermal fluctuation at that location (Fig. 1c). The root-mean-square (rms) value of the five thermistors' measured fluctuations is calculated to estimate the characteristic temporally and spatially averaged temperature fluctuation, θ , in the convecting fluid bulk. The equation is thus given as

$$\theta = \sqrt{\frac{1}{5N_t} \sum_{i=1}^5 \sum_{j=1}^{N_t} (T_{i,j} - \bar{T}_i)^2}. \quad (12)$$

This value is then normalized by ΔT in our analysis.

The vertical flow velocity, u_z , is measured using an ultrasonic Doppler velocimeter (UDV). For these experiments, three vertically oriented transducer probes are embedded within the top thermal block of the convection cell, as shown in Fig. 1b and Supplementary Fig. 4c. They are each in direct contact with the liquid gallium, which contains oxides that are acoustically sensed by the UDV (Wang and Kelley, 2021). The UDV velocities are recorded at approximately 2 mm increments across the entire vertical length of the cell at an approximately 10 Hz date rate (Vogt et al., 2018, 2021); see Fig. 1b. The characteristic u_z velocity is calculated as a spatiotemporal rms, using UDV data from the middle 50% of the cell height ($h = 0.25H$ to $0.75H$)

(Fig. 1), following

$$u_z = \sqrt{\frac{1}{N_z N_t} \sum_{i=1}^{N_z} \sum_{j=1}^{N_t} u_{i,j}^2}, \quad (13)$$

where $u_{i,j}$ is each velocity measurement at space element i and time element j . The length of the time series is represented by N_t and the length of the spatial array is given by N_z .

Modes of convection. Convective instabilities arise in a number of different ways in rotating systems. Here, three modes of convection are relevant to the experiments conducted.

The primary mode is known as the *steady* or *stationary mode*. This type of instability occurs when thermal buoyancy overcomes the stabilizing effect of rotation, such that fluid warmed by bottom boundary rises, and fluid cooled by the top boundary sinks. This mode is therefore fueled by thermal fluxes through the boundaries. The critical value of Ra for which steady convection onsets is dependent on the Ekman number following

$$Ra_S^\infty = 8.7E^{-4/3} \quad (14)$$

in a horizontal plane layer in the limit of infinitely low E (Chandrasekhar, 1961; Aurnou et al., 2018), or

$$Ra_S = (8.7 - 9.63E^{1/6})E^{-4/3} \quad (15)$$

for a planar system rotating at a finite rate ($E > 0$) and no-slip top and bottom boundaries (Niiler and Bisshopp, 1965; Kunen, 2021). In this work, expression (15) is employed.

In systems with lateral boundaries, convective instabilities additionally develop at the sidewall in the form of waves of alternating upward and downward flow that travel around the perimeter of the cell. These are known as *wall modes*. For a no-slip, thermally insulated system, wall modes are predicted to onset at a critical Rayleigh number given by

$$Ra_W = \pi^2 \sqrt{6\sqrt{3}E^{-1} + 46.55E^{-2/3}} \quad (16)$$

(Zhang and Liao, 2009). These modes are strongest at the periphery of the tank and aren't expected to significantly affect the bulk interior flow quantities (i.e., u_z , θ). However, they do contribute to the total global heat transport (Nu) for the system.

Specific to rotating fluids with $Pr < 0.68$, convective instability can also develop in the form of thermally driven inertial oscillations known as *oscillatory modes* (Zhang and Roberts, 1997). This instability onsets at a lower Ra than the critical value for steady modes. The prediction for onset in a horizontally infinite plane layer follows

$$Ra_O^\infty = 17.4 \left(\frac{E}{Pr} \right)^{-4/3} \quad (17)$$

(Chandrasekhar, 1961). Oscillatory onset predictions in finite cylindrical geometry subject to non-slip experimental boundary conditions, Ra_O^{cyl} , are given in Zhang and Liao (2009), verified through comparisons with simulations at $E = 10^{-4}$, $\Gamma = 2$ and $10^{-6} \leq Pr \leq 0.05$. In contrast to steady and wall modes, which

are directly linked to the system boundaries, oscillatory modes are driven by the internal temperature gradient, and are therefore independent of the boundaries. Isolating the oscillatory mode can uniquely enable convection that is free from diffusive boundary effects.

Taking the ratio of the critical onset prediction for the stationary mode to that of the oscillatory mode gives

$$\frac{Ra_S^\infty}{Ra_O^\infty} = \frac{1}{2} Pr^{-4/3}. \quad (18)$$

Equation (18) shows that the smaller the Prandtl number is, the larger the separation between the onset of each mode. Liquid gallium, at $Pr \approx 0.027$, yields $Ra_S^\infty/Ra_O^\infty \approx 60$, so we can access oscillatory-dominated convection for approximately 1-2 orders of magnitude in the Rayleigh number. Fluids with smaller Prandtl numbers, such as liquid sodium with $Pr \approx 0.001$, would provide an even larger range in which oscillatory convection can be studied with $Ra_S^\infty/Ra_O^\infty \approx 10^3$, yielding approximately 3 orders of magnitude in Ra before steady convection onsets.

The ratio of the wall mode onset prediction to that of the oscillatory mode simplifies to

$$\frac{Ra_W}{Ra_O^\infty} = (1.83E^{1/3} + 2.74E^{2/3}) Pr^{-4/3}. \quad (19)$$

According to (19), the Ekman number needs to be moderately large to isolate oscillatory modes from wall modes in low Pr fluids. This could be achieved with relatively slow rotation, or preferably, with relatively small H , which would additionally aid in keeping Ra below Ra_S . Further, convection cells with small H and large D (yielding larger aspect ratio $\Gamma = D/H$) will better isolate oscillatory behavior because they mitigate effects from wall modes. The contribution from wall modes to convective heat transfer increases with increasing sidewall curvature. Supplementary Table 3 includes the supercriticality values for steady, wall, and oscillatory modes for all rotating cases.

Regime transitions. Thermal inertial oscillatory bulk dynamics dominate our data from just after the onset of convection (Horn and Schmid, 2017; Aurnou et al., 2018; Cheng et al., 2018; Vogt et al., 2021). A change in scaling behavior is found for sufficiently strong thermal forcing (Ra) near the onset of the (non-oscillatory) stationary mode of rotating convection.

Supplementary Figs. 6a, 6b, and 6c show measured Ro_z , $\theta/\Delta T$, and $Nu - 1$, against the supercriticality determined by the steady mode, Ra/Ra_S . The marker notations are the same as that of Fig. 3, but vertical dotted lines are added to mark $Ra/Ra_S = 1$. This simple demarcation works well to separate the distinctly different slope of the asymptotic regime in the data for $\theta/\Delta T$ and $Nu - 1$, though it is less clear in indicating behavioral shifts in the Ro_z data.

Supplementary Figs. 6d, 6e, and 6f show the same data against the convective Rossby number, Ro_c . The vertical dotted lines mark $Ro_c = 1$, which has also been argued as a regime bound for rotational effects (King and Aurnou, 2013, 2015). Across all three datasets, there lacks a clear transition at a consistent value of Ro_c . There is also an aspect-ratio effect present that is instead better captured by Ra/Ra_S .

Based on Supplementary Fig. 6, we analyze the best fit scaling behaviors in our liquid metal rotating convection data using laboratory data in the $1.5Ra_O^{cyl} < Ra < Ra_S$ range at each rotation rate (E) investigated.

Fundamental balances. The asymptotic scaling prediction for diffusivity-free heat transfer in rotating convection is

$$Nu - 1 = C_J Ra^{3/2} E^2 Pr^{-1/2}, \quad (20)$$

where $C_J \approx 1/25$ is a constant estimated in the asymptotically-reduced modeling study of Julien et al. (2012).

Non-diffusive momentum transfer is determined from a triple balance between the Coriolis, inertia, and buoyancy terms of the vorticity equation, defining a ‘CIA’ prediction for the Reynolds number that yields

$$Re = C_1 \left(\frac{Ra(Nu - 1)}{Pr^2} \right)^{2/5} E^{1/5} \quad (21)$$

(Ingersoll and Pollard, 1982; Cardin and Olson, 1994; Aubert et al., 2001; King et al., 2013; Guervilly et al., 2019; Aurnou et al., 2020; Kolhey et al., 2022; Oliver et al., 2023; Hawkins et al., 2023; Abbate and Aurnou, 2023). Further, CIA scaling arguments (Aubert et al., 2001; Abbate and Aurnou, 2023) also yield predictions for the diffusion-free rotating convective temperature perturbations in the fluid bulk, θ , as

$$\frac{\theta}{\Delta T} = C_2 \left(\frac{Nu - 1}{RaE} \right)^{3/5} Ro_c^{2/5}. \quad (22)$$

Substituting the asymptotic heat transfer scaling (20) into the CIA predictions (21) and (22) yields estimates for the nondimensional velocity, Re , and the nondimensional temperature perturbation, $\theta/\Delta T$, in the asymptotic, diffusivity-free regime:

$$Re = C_1 C_J^{2/5} Ro_c^2 E^{-1}, \quad (23)$$

$$\frac{\theta}{\Delta T} = C_2 C_J^{3/5} Ro_c. \quad (24)$$

Substituting $Re = Ro/E$ into the Reynolds number prediction yields

$$Ro = C_1 C_J^{2/5} Ro_c^2, \quad (25)$$

where $Ro = u/(2\Omega H)$ is the Rossby number. Interestingly, the asymptotic scalings (24) and (25) both depend only on the convective Rossby number, $Ro_c = (RaE^2/Pr)^{1/2}$ (cf. Aurnou et al., 2020; Abbate and Aurnou, 2023). Setting $C_J \approx 1/25$ in (20), $C_J^{2/5} \approx (1/25)^{2/5} = 0.276$ in (23), $C_J^{3/5} \approx (1/25)^{3/5} = 0.145$ in (24), and assuming $C_1 \approx C_2 \approx 1$ for simplicity, we arrive at the quantitative asymptotically reduced modeling predictions for the heat transfer, momentum transfer, and bulk thermal anomalies, respectively, against which we compare our laboratory liquid metal rotating convection data in Fig. 3 and Table 2. Our results in Table 2 show that actual values are $C_1 = 1.50 \pm 0.58$ and $C_2 = 2.69 \pm 0.35$ for the $\Gamma \approx 1/2$ tank, and $C_1 = 2.21 \pm 0.88$ and $C_2 = 1.46 \pm 0.16$ for the $\Gamma \approx 2$ tank, which are consistent with order unity.

Earth core calculations. In this work, we have used a ΔT -based framework, but the thermal flux is often what is most easily measured in most geophysical and astrophysical cases. In this case, the diffusivity-free heat transfer prediction can instead be used to predict the Rayleigh number, Ra , from a given flux-based Rayleigh number, Ra_F . Substituting (20) into $Ra_F = Ra(Nu - 1)$ gives

$$Ra_F = C_J Ra^{5/2} E^2 Pr^{-1/2}, \quad (26)$$

which we can re-order as

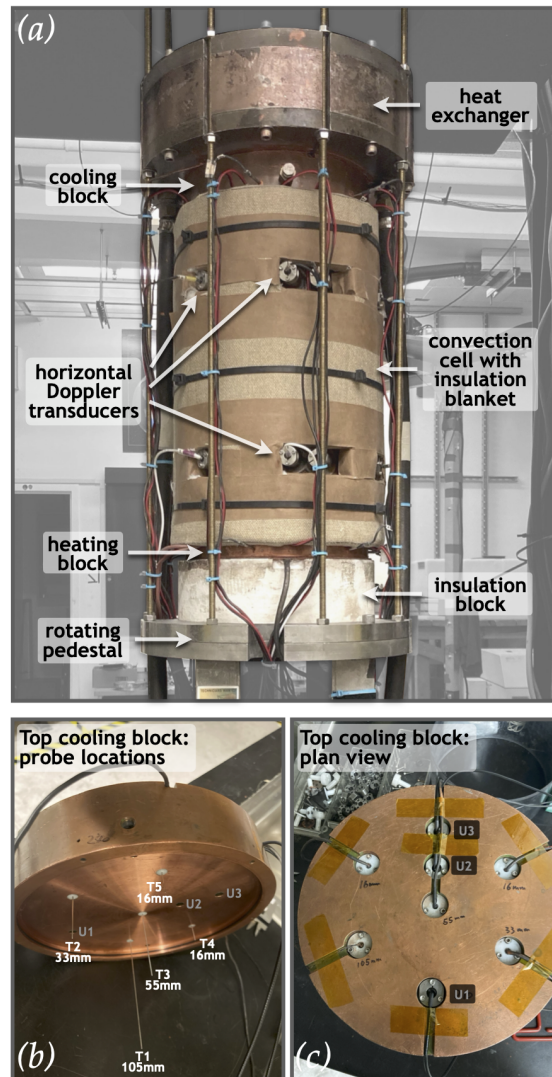
$$Ra = C_J^{-2/5} Ra_F^{2/5} E^{-4/5} Pr^{1/5}. \quad (27)$$

The diffusivity-free velocity prediction can also be re-arranged for the Rayleigh number. Substituting the definition for the convective Rossby number, $Ro_c = (RaE^2/Pr)^{1/2}$, and re-arranging yields

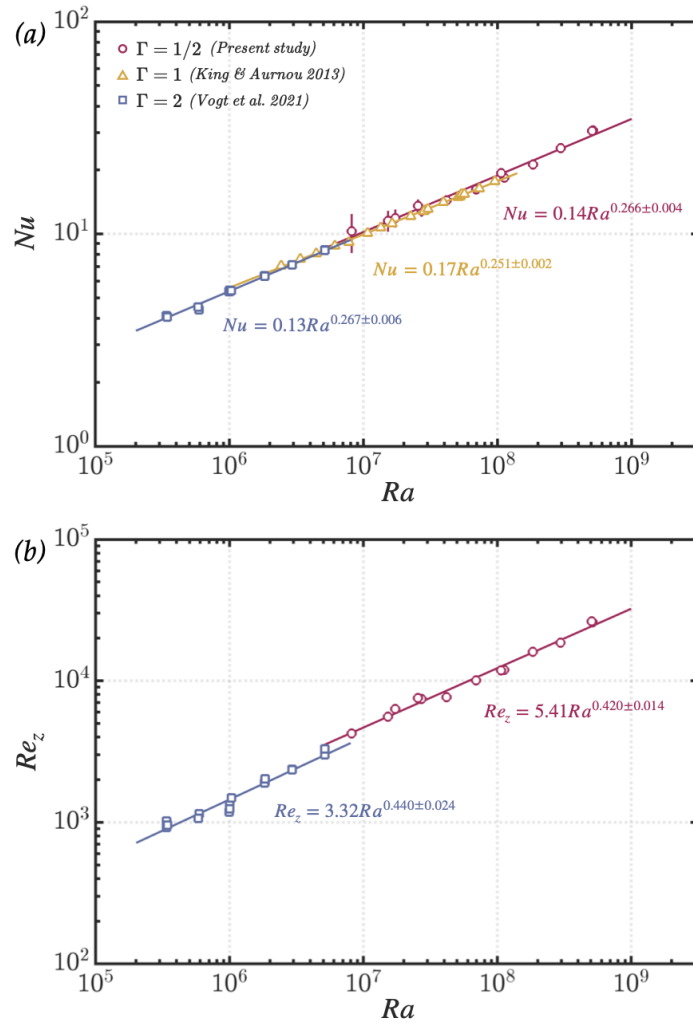
$$Ra = C_J^{-2/5} Re E^{-1} Pr. \quad (28)$$

This provides two independent predictions for the Rayleigh number based on heat flux and velocity estimates for the geophysical or astrophysical system.

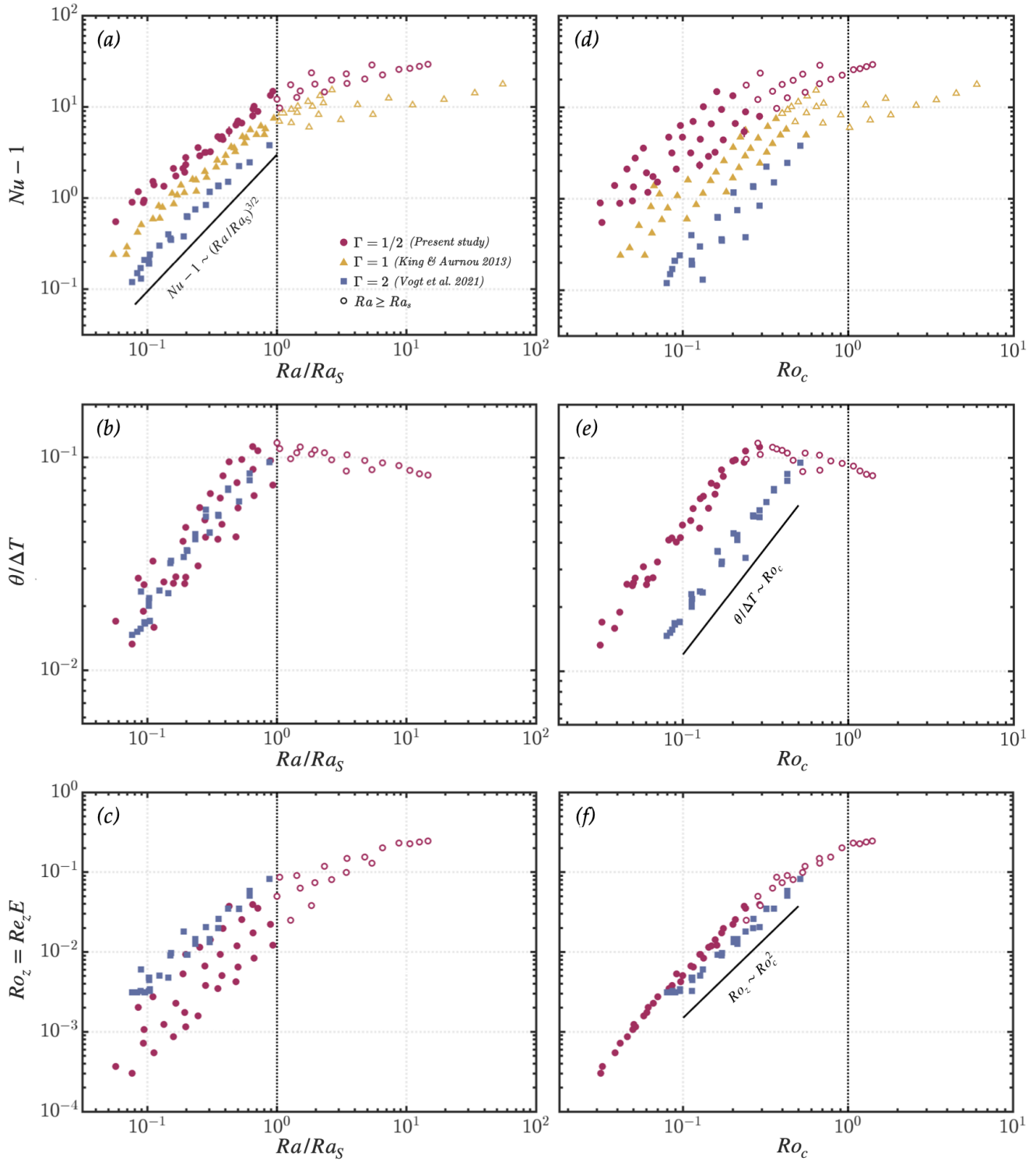
Supplementary Items



Supplementary Figure 4: Experimental apparatus. (a) Rotating convection cell. The cylindrical tank is $H = 40.0$ cm tall by $D = 19.68$ cm wide (aspect ratio $= \Gamma = D/H \approx 1/2$) and filled with liquid gallium ($Pr \approx 0.027$). Heat is supplied from a non-inductively wound heating pad through the bottom copper 'heating' block, and extracted by a heat exchanger plate in contact with the top copper 'cooling' block, to generate axially-aligned thermal buoyancy-driven convection. The cell is mounted on a rotating pedestal to rotate the cell about its vertical axis. An insulation blanket surrounds the cell to mitigate heat losses. (b) Underside of the top copper 'cooling block'. Five internal thermistors of varied lengths are positioned within the fluid to measure internal temperatures. Three ultrasonic Doppler transducers are embedded vertically in the copper block to measure fluid velocities. The face of the transducer is in contact with the liquid gallium and pointed straight from the top of the cell towards the bottom.



Supplementary Figure 5: Non-rotating RBC data for each of the three cells used in the rotating study. (a) Heat transfer efficiency, Nu , and **(b)** dimensionless vertical velocity, Re_z , each versus buoyancy forcing, Ra . Solid lines indicate the power-law best fit to each dataset. Data for the $\Gamma \approx 1/2$ cell is included in Supplementary Table 3, data for the $\Gamma \approx 1$ cell is included in King and Aurnou (2015), and data for the ($\Gamma \approx 2$) cell is included in Vogt et al. (2018).



Supplementary Figure 6: Tests of transition values at which scaling behavior deviates from the diffusion-free predictions. Panels (a), (b), and (c) demonstrate a transition at approximately $Ra = Ra_S$ for Ro_z , $\theta/\Delta T$, and Nu , respectively, which is marked by a vertical dotted line. Panels (d), (e), and (f) show a lack of transition at $Ro_c = 1$ for the same quantities, also marked by a dotted line. Solid diagonal lines in panels (c), (d), and (e) indicate the diffusivity-free predictions.

Supplementary Table 3: Liquid gallium data for the $\Gamma \approx 1/2$ cell.

E	Ra	Pr	Nu	$\theta/\Delta T$	Re_z	Ra/Ra_S	Ra/Ra_O^{cyl}	Ra/Ra_W
∞	8.13E+06	0.028	10.3	9.68E-02	4.25E+03	–	–	–
∞	1.52E+07	0.028	11.5	9.29E-02	5.58E+03	–	–	–
∞	1.72E+07	0.028	11.9	1.01E-01	6.32E+03	–	–	–
∞	2.71E+07	0.027	12.9	9.19E-02	7.47E+03	–	–	–
∞	2.55E+07	0.028	13.6	1.02E-01	7.55E+03	–	–	–
∞	4.16E+07	0.027	14.4	8.85E-02	7.66E+03	–	–	–
∞	6.93E+07	0.027	16.2	8.16E-02	1.01E+04	–	–	–
∞	1.13E+08	0.027	18.4	7.82E-02	1.20E+04	–	–	–
∞	1.06E+08	0.027	19.4	9.22E-02	1.18E+04	–	–	–
∞	1.84E+08	0.027	21.3	7.89E-02	1.61E+04	–	–	–
∞	2.96E+08	0.026	25.3	7.96E-02	1.86E+04	–	–	–
∞	5.16E+08	0.024	30.7	7.77E-02	2.59E+04	–	–	–
∞	5.08E+08	0.025	30.6	7.58E-02	2.63E+04	–	–	–
1.09E-05	1.95E+07	0.028	8.94	1.13E-01	3.59E+03	0.65	10.2	6.48
1.08E-05	1.30E+07	0.028	6.41	9.53E-02	3.46E+03	0.43	6.67	4.27
1.07E-05	7.14E+07	0.027	15.6	1.05E-01	1.11E+04	2.32	36.6	23.3
1.07E-05	4.37E+07	0.027	13.7	1.05E-01	8.50E+03	1.42	22.4	14.3
1.07E-05	3.24E+07	0.027	10.8	1.10E-01	8.05E+03	1.05	16.6	10.6
1.05E-05	1.09E+08	0.027	19.1	1.03E-01	1.41E+04	3.46	55.7	35.0
1.05E-05	2.05E+08	0.027	23.4	9.44E-02	1.92E+04	6.51	105	65.8
1.05E-05	1.50E+08	0.027	21.2	9.67E-02	1.47E+04	4.75	76.6	48.1
1.04E-05	2.80E+08	0.026	26.7	9.17E-02	2.23E+04	8.71	145	88.6
1.04E-05	3.42E+08	0.026	27.3	8.69E-02	2.20E+04	10.6	174	108
1.01E-05	4.19E+08	0.026	28.7	8.38E-02	2.37E+04	12.6	212	129
9.77E-06	5.12E+08	0.025	30.3	8.27E-02	2.53E+04	14.7	257	153
5.15E-06	1.65E+07	0.028	3.33	4.70E-02	1.82E+03	0.20	3.43	2.61
5.13E-06	3.21E+07	0.028	5.40	8.20E-02	3.83E+03	0.38	6.65	5.05
5.13E-06	2.12E+07	0.028	3.91	5.82E-02	2.24E+03	0.25	4.41	3.34
5.11E-06	4.52E+07	0.027	7.67	9.78E-02	4.96E+03	0.54	9.37	7.09
5.11E-06	2.58E+07	0.027	4.23	6.76E-02	2.80E+03	0.30	5.34	4.04
5.11E-06	6.01E+07	0.027	9.91	1.08E-01	6.91E+03	0.71	12.5	9.43
5.06E-06	8.57E+07	0.027	13.1	1.17E-01	9.84E+03	1.00	17.7	13.3
5.01E-06	1.31E+08	0.027	16.0	1.12E-01	1.26E+04	1.51	26.9	20.1
5.01E-06	1.70E+08	0.027	18.7	1.09E-01	1.47E+04	1.95	35.0	26.1

Continued on next page

Supplementary Table 3 – continued from previous page

E	Ra	Pr	Nu	$\theta/\Delta T$	Re_z	Ra/Ra_S	Ra/Ra_O^{cyl}	Ra/Ra_W
4.94E-06	2.34E+08	0.027	20.8	9.77E-02	1.63E+04	2.64	48.1	35.4
4.87E-06	3.10E+08	0.026	24.1	8.63E-02	2.05E+04	3.44	63.4	46.3
4.59E-06	5.28E+08	0.025	29.8	8.75E-02	2.81E+04	5.39	107	74.3
2.04E-06	3.25E+07	0.028	2.53	3.26E-02	1.34E+03	0.11	2.31	2.05
2.04E-06	2.51E+07	0.028	2.17	2.71E-02	9.92E+02	0.09	1.79	1.58
2.03E-06	5.54E+07	0.027	3.11	4.04E-02	2.62E+03	0.19	3.95	3.48
2.02E-06	8.28E+07	0.027	4.18	5.09E-02	3.31E+03	0.28	5.89	5.16
2.02E-06	1.09E+08	0.027	5.47	6.46E-02	4.62E+03	0.36	7.75	6.79
1.99E-06	1.49E+08	0.027	7.57	7.63E-02	5.96E+03	0.49	10.6	9.18
1.97E-06	2.01E+08	0.027	10.5	8.81E-02	8.81E+03	0.65	14.2	12.2
1.96E-06	2.77E+08	0.026	14.3	9.67E-02	1.13E+04	0.89	19.5	16.7
1.92E-06	4.08E+08	0.026	18.4	9.88E-02	1.31E+04	1.27	28.6	24.2
1.80E-06	6.43E+08	0.024	24.7	1.04E-01	2.12E+04	1.84	44.5	35.8
8.77E-07	1.52E+08	0.027	2.75	2.75E-02	2.61E+03	0.17	3.93	4.15
8.69E-07	8.82E+07	0.027	1.94	2.53E-02	1.22E+03	0.09	2.23	2.38
8.44E-07	2.73E+08	0.026	4.18	4.22E-02	4.53E+03	0.28	6.87	7.14
8.37E-07	3.70E+08	0.026	5.73	4.85E-02	6.04E+03	0.38	9.31	9.62
8.17E-07	5.08E+08	0.026	8.01	5.80E-02	7.96E+03	0.50	12.7	12.9
8.03E-07	6.93E+08	0.025	11.1	6.61E-02	1.04E+04	0.66	17.3	17.2
7.77E-07	1.01E+09	0.024	15.8	7.43E-02	1.57E+04	0.93	25.5	24.4
5.12E-07	2.56E+08	0.027	2.35	2.60E-02	2.41E+03	0.13	3.40	4.07
5.09E-07	1.10E+08	0.027	1.55	1.70E-02	7.27E+02	0.06	1.42	1.73
5.03E-07	1.82E+08	0.027	1.89	1.90E-02	1.43E+03	0.09	2.35	2.85
4.90E-07	3.93E+08	0.026	2.92	2.55E-02	3.59E+03	0.19	5.05	5.98
4.81E-07	7.26E+08	0.025	5.72	4.13E-02	7.24E+03	0.35	9.54	10.9
4.51E-07	1.09E+09	0.024	7.30	4.23E-02	9.41E+03	0.48	13.8	15.4
2.89E-07	3.16E+08	0.026	1.90	1.33E-02	1.05E+03	0.08	2.15	2.84
2.83E-07	4.80E+08	0.026	2.40	1.59E-02	1.94E+03	0.11	3.25	4.23
2.74E-07	7.03E+08	0.025	3.12	2.57E-02	3.17E+03	0.16	4.73	6.01
2.70E-07	8.93E+08	0.025	3.79	2.74E-02	4.29E+03	0.20	5.99	7.52
2.66E-07	1.14E+09	0.024	4.57	3.09E-02	5.96E+03	0.25	7.61	9.44

References

- K. Moffatt, E. Dormy, *Self-exciting fluid dynamos*, volume 59, Cambridge University Press, 2019.
- G. Ahlers, S. Grossmann, D. Lohse, Heat transfer and large scale dynamics in turbulent Rayleigh–Bénard convection, *Rev. Mod. Phys.* 81 (2009) 503.
- R. E. Ecke, O. Shishkina, Turbulent rotating Rayleigh–Bénard convection, *Ann. Rev. Fluid Mech.* 55 (2023) 603–638.
- R. H. Kraichnan, Turbulent thermal convection at arbitrary Prandtl number, *Phys. Fluids* 5 (1962) 1374–1389.
- E. A. Spiegel, Convection in stars I. Basic Boussinesq convection, *Annu. Rev. Astron. Astrophys.* 9 (1971) 323–352.
- D. J. Stevenson, Turbulent thermal convection in the presence of rotation and a magnetic field: a heuristic theory, *Geophys. Astrophys. Fluid Dyn.* 12 (1979) 139–169.
- U. R. Christensen, J. Aubert, Scaling properties of convection-driven dynamos in rotating spherical shells and application to planetary magnetic fields, *Geophys. J. Int.* 166 (2006) 97–114.
- M. Plumley, K. Julien, Scaling laws in Rayleigh–Bénard convection, *Earth Space Sci.* 6 (2019) 1580–1592.
- J. A. Abbate, J. M. Aurnou, Rotating convective turbulence in moderate to high Prandtl number fluids, *Geophys. Astrophys. Fluid Dyn.* (2023) 1–40.
- K. Julien, E. Knobloch, A. M. Rubio, G. M. Vasil, Heat transport in low-Rossby-number Rayleigh–Bénard convection, *Phys. Rev. Lett.* 109 (2012) 254503.
- A. P. Ingersoll, D. Pollard, Motion in the interiors and atmospheres of Jupiter and Saturn: Scale analysis, anelastic equations, barotropic stability criterion, *Icarus* 52 (1982) 62–80.
- K. M. Soderlund, B. E. Schmidt, J. Wicht, D. D. Blankenship, Ocean-driven heating of Europa’s icy shell at low latitudes, *Nature Geosci.* 7 (2014) 16–19.
- E. M. King, J. M. Aurnou, Thermal evidence for Taylor columns in turbulent rotating Rayleigh–Bénard convection, *Phys. Rev. E* 85 (2012) 016313.
- K. Julien, J. M. Aurnou, M. A. Calkins, E. Knobloch, P. Marti, S. Stellmach, G. M. Vasil, A nonlinear model for rotationally constrained convection with Ekman pumping, *J. Fluid Mech.* 798 (2016) 50–87.
- K. Zhang, X. Liao, *Theory and modeling of rotating fluids: convection, inertial waves and precession*, Cambridge University Press, 2017.
- J. M. Aurnou, V. Bertin, A. M. Grannan, S. Horn, T. Vogt, Rotating thermal convection in liquid gallium: Multi-modal flow, absent steady columns, *J. Fluid Mech.* 846 (2018) 846–876.
- T. G. Oliver, A. S. Jacobi, K. Julien, M. A. Calkins, Small scale quasi-geostrophic convective turbulence at large Rayleigh number, *Phys. Rev. Fluids* 8 (2023) 093502.
- R. E. Ecke, F. Zhong, E. Knobloch, Hopf bifurcation with broken reflection symmetry in rotating Rayleigh–Bénard convection, *Europhys. Lett.* 19 (1992) 177.
- A. J. Barker, A. M. Dempsey, Y. Lithwick, Theory and simulations of rotating convection, *Astrophys. J.* 791 (2014) 13.
- S. Zou, Y. Yang, Realizing the ultimate scaling in convection turbulence by spatially decoupling the thermal and viscous boundary layers, *J. Fluid Mech.* 919 (2021) R3.
- S. Lepot, S. Aumaître, B. Gallet, Radiative heating achieves the ultimate regime of thermal convection, *Proc. Natl. Acad. Sci. USA* 115 (2018) 8937–8941.
- V. Bouillaut, B. Miquel, K. Julien, S. Aumaître, B. Gallet, Experimental observation of the geostrophic turbulence regime of rapidly rotating convection, *Proc. Natl. Acad. Sci. USA* 118 (2021) e2105015118.
- B. Favier, E. Knobloch, Robust wall states in rapidly rotating Rayleigh–Bénard convection, *J. Fluid Mech.* 895 (2020) R1.
- X. M. de Wit, A. J. A. Guzmán, M. Madonia, J. S. Cheng, H. J. Clercx, R. P. J. Kunnen, Turbulent rotating convection confined in a slender cylinder: the sidewall circulation, *Phys. Rev. Fluids* 5 (2020) 023502.
- X. Zhang, R. E. Ecke, O. Shishkina, Boundary zonal flows in rapidly rotating turbulent thermal convection, *J. Fluid Mech.* 915 (2021) A62.
- H. Y. Lu, G. Y. Ding, J. Q. Shi, K. Q. Xia, J. Q. Zhong, Heat-transport scaling and transition in geostrophic rotating convection with varying aspect ratio, *Phys. Rev. Fluids* 6 (2021) L071501.
- M. Madonia, A. J. A. Guzmán, H. J. Clercx, R. P. J. Kunnen, Reynolds number scaling and energy spectra in geostrophic convection, *J. Fluid Mech.* 962 (2023) A36.
- S. Chandrasekhar, *Hydrodynamic and hydromagnetic stability*, Oxford, UK, 1961.
- K. Zhang, P. H. Roberts, Thermal inertial waves in a rotating fluid layer: exact and asymptotic solutions, *Phys. Fluids* 9 (1997) 1980–1987.
- K. Zhang, X. Liao, The onset of convection in rotating circular cylinders with experimental boundary conditions, *J. Fluid Mech.* (2009).
- S. Horn, P. J. Schmid, Prograde, retrograde, and oscillatory modes in rotating Rayleigh–Bénard convection, *J. Fluid Mech.* 831 (2017) 182–211.
- E. M. King, J. M. Aurnou, Turbulent convection in liquid metal with and without rotation, *Proc. Natl. Acad. Sci. USA* 110 (2013) 6688–6693.
- T. Vogt, S. Horn, J. M. Aurnou, Oscillatory thermal–inertial flows in liquid metal rotating convection, *J. Fluid Mech.* 911 (2021) A5.
- B. Wang, D. H. Kelley, Microscale mechanisms of ultrasound velocity measurement in metal melts, *Flow Meas.* 81 (2021) 102010.
- E. M. King, J. M. Aurnou, Magnetostrophic balance as the optimal state for turbulent magnetoconvection, *Proc. Natl. Acad. Sci. USA* 112 (2015) 990–994.
- P. P. Niiler, F. E. Bisschopp, On the influence of Coriolis force on onset of thermal convection, *J. Fluid Mech.* 22 (1965) 753–761.
- R. P. J. Kunnen, The geostrophic regime of rapidly rotating turbulent convection, *J. Turb.* 22 (2021) 267–296.
- C. A. Jones, D. R. Moore, N. O. Weiss, Axisymmetric convection in a cylinder, *J. Fluid Mech.* 73 (1976) 353–388.
- A. Chiffaudel, S. Fauve, B. Perrin, Viscous and inertial convection at low Prandtl number: Experimental study, *Europhys. Lett.* 4 (1987) 555.
- R. Holme, P. Olson, G. Schubert, Large-scale flow in the core, *Treatise on geophysics* 8 (2015) 107–130.
- K. M. Soderlund, M. Rovira-Navarro, M. Le Bars, B. E. Schmidt, T. Gerkema, The physical oceanography of ice-covered moons, *Annu. Rev. Mar. Sci.* 16 (2024) 25–53.
- G. M. Vasil, K. Julien, N. A. Featherstone, Rotation suppresses giant-scale solar convection, *Proc. Natl. Acad. Sci. USA* 118 (2021) e2022518118.
- P. Olson, *Core Dynamics: An Introduction and Overview*, *Treatise on geophysics* 8 (2015) 1–25.
- L. Terrien, B. Favier, E. Knobloch, Suppression of wall modes in rapidly rotating Rayleigh–Bénard convection by narrow horizontal fins, *Phys. Rev. Lett.* 130 (2023) 174002.
- T. Vogt, S. Horn, A. M. Grannan, J. M. Aurnou, Jump rope vortex in liquid metal convection, *Proc. Natl. Acad. Sci. USA* 115 (2018) 12674–12679.
- A. M. Grannan, J. S. Cheng, A. Aggarwal, E. K. Hawkins, Y. Xu, S. Horn, J. Sánchez-Álvarez, J. M. Aurnou, Experimental pub crawl from Rayleigh–Bénard to magnetostrophic convection, *J. Fluid Mech.* 939 (2022) R1.
- Y. Xu, S. Horn, J. M. Aurnou, Thermoelectric precession in turbulent magnetoconvection, *J. Fluid Mech.* 930 (2022) A8.
- Y. Xu, S. Horn, J. M. Aurnou, Transition from wall modes to multimodality in liquid gallium magnetoconvection, *Phys. Rev. Fluids* 8 (2023) 103503.
- E. M. King, S. Stellmach, J. M. Aurnou, Heat transfer by rapidly rotating Rayleigh–Bénard convection, *J. Fluid Mech.* 691 (2012) 568–582.
- J. S. Cheng, J. M. Aurnou, K. Julien, R. P. J. Kunnen, A heuristic framework for next-generation models of geostrophic convective turbulence, *Geophys. Astrophys. Fluid Dyn.* 112 (2018) 277–300.
- P. Cardin, P. Olson, Chaotic thermal convection in a rapidly rotating spherical shell: consequences for flow in the outer core, *Phys. Earth Planet. Inter.* 82 (1994) 235–259.
- J. Aubert, D. Brito, H. Nataf, P. Cardin, J. Masson, A systematic experimental study of rapidly rotating spherical convection in water and liquid gallium, *Phys. Earth Planet. Inter.* 128 (2001) 51–74.
- E. M. King, S. Stellmach, B. Buffett, Scaling behaviour in Rayleigh–Bénard convection with and without rotation, *J. Fluid Mech.* 717 (2013) 449–471.
- C. Guervilly, P. Cardin, N. Schaeffer, Turbulent convective length scale in planetary cores, *Nature* 570 (2019) 368–371.
- J. M. Aurnou, S. Horn, K. Julien, Connections between nonrotating, slowly rotating, and rapidly rotating turbulent convection transport scalings, *Phys. Rev. Res.* 2 (2020) 043115.
- P. Kolhey, S. Stellmach, D. Heyner, Influence of boundary conditions on rapidly rotating convection and its dynamo action in a plane fluid layer, *Phys. Rev. Fluids* 7 (2022) 043502.
- E. K. Hawkins, J. S. Cheng, J. A. Abbate, T. Pilegard, S. Stellmach, K. Julien, J. M. Aurnou, Laboratory models of planetary core-style convective turbulence, *Fluids* 8 (2023) 106.